Dear,

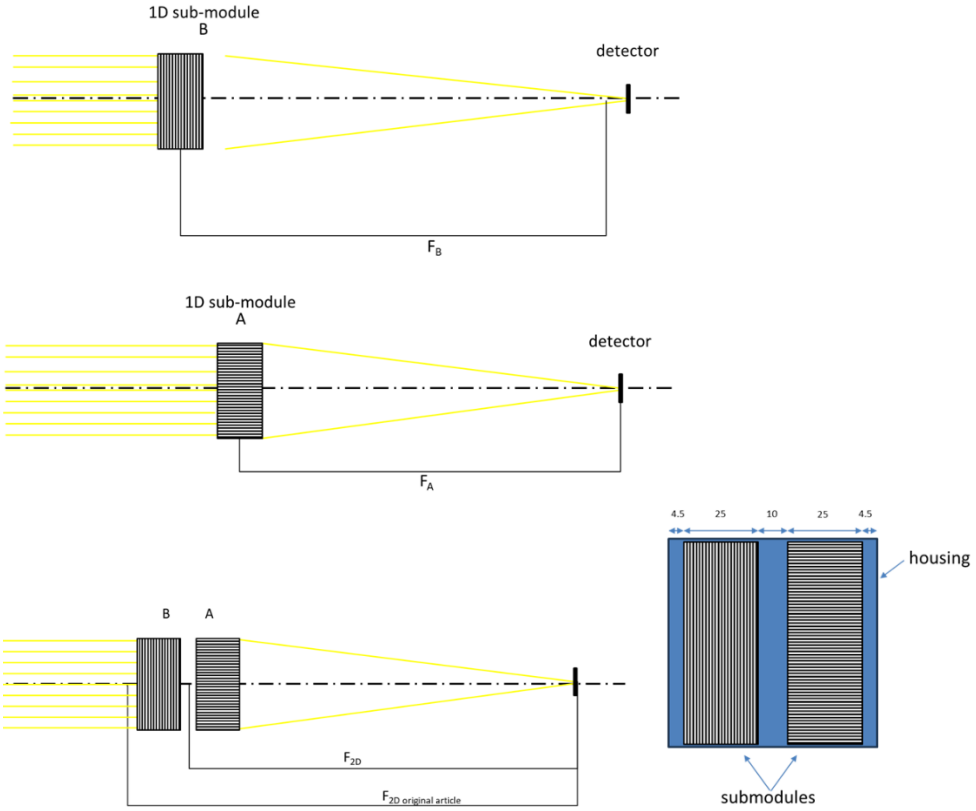
thank you for the careful reading and constructive feedback. We address each point below and have revised the manuscript accordingly.

1. Page 1, Sec 1, line 1, the word 'optical' in 'an optical X-ray payload' should be deleted to avoid confusion. DONE
2. Page 2, Sec 2, paragraph 6, line 2, a word 'It' should be added after '2025.', and it would be nice to update the SMILE launch scheduled in 2025, since now it's already Oct 2025. DONE
3. Page 2, the bottom line, a sketch figure to show 'a uniform radial pattern along the perimeter of a spherical surface with radius R' will be very much helpful for readers to understand better the design. Fig 1 in page 3 does not provide such information. DONE Added the figure.
4. Page 4, Fig 2, in the caption it would be nice to describe (identify) more explicitly all the major parts in the figure. Same for Fig 8 in page 8. DONE – fig 2 and 8
5. Page 8, fig 9, what is the energy used for this figure? NiP has 3 different energies, as listed in Table 2. Figure 9 was acquired with the Rigaku CMOS camera, which is not energy-resolving; it integrates the signal over the full source spectrum and therefore a single energy from Table 2 cannot be assigned to this image. Clarification: In our laboratory spectrum the most pronounced contribution is at 0.85 keV, so the image contrast in Fig. 9 is dominated by ~0.85 keV photons.
   Updated: The measurements revealed consistent FWHM values and stable optical performance for all available energies from Ti, Ag, and NiP targets (Table~\ref{FWHM_comparison}). The best images of the focal spot were obtained at all available energies using a Rigaku camera. Data acquired with a nonenergy resolving CMOS detector (Rigaku); the signal is integrated over the source spectrum. The dominant contribution to the image is from the 0.85 keV line.
6. Page 9, Fig 10, the abscissa of the two right columns is always 'x'. It's probably a typo. And, which energy is it with NiP? DONE, NiP – see 4
7. Page 10, Fig 12, the curve for the direct beam (source) is barely visible. DONE, log scale was used
8. Page 10, Table 4, why is the normalized gain in 1.85-2.25 keV for the direct beam not 1? Updated and clarified
   For the NiP target we normalize spectra to the area under the Ni Kα peak, integrating over 7.30–7.70 keV (which brackets Ni Kα at ≈7.48 keV). Specifically, for each spectrum we scale the data so that the integral in this window equals 1. The normalized gain reported in Tables 4 is then computed as a ratio of band integrals relative to the Ni Kα window, referenced to the direct beam:

$$G_{\mathrm{norm}}(b) = \frac{\int_b S_{\mathrm{opt}}(E)\,dE \,/\, \int_{7.30-7.70} S_{\mathrm{opt}}(E)\,dE}{\int_b S_{\mathrm{dir}}(E)\,dE \,/\, \int_{7.30-7.70} S_{\mathrm{dir}}(E)\,dE}.$$

9. Page 11, Table 5, the energy dependence requires some explanations. It seems the best focal length is somewhat longer for 4.5 keV.
   In the original plots, the detector distance was measured from the edge of the optics/submodules during measurement. We re-referenced all distances to the

submodule or 2D optics midplane, consistent with Sec. 3 or Fig. 7 (please see F_A, F_B and F_{2D}), and updated Figs. 9, 11, and 13 and Tab 1.
For better understanding:



Added (section 6.1) X-ray vacuum testing was conducted to verify the key optical parameters of the LE system. Measurements were taken separately for each one-dimensional (1D) sub-module and then for the full two-dimensional (2D) assembly. To comply with the 4U CubeSat envelope (100 × 100 × 400 mm), the design nominal focal lengths were set to \(F_A = 347.5~\mathrm{mm}\) and \(F_B = 382.5~\mathrm{mm}\) (distances referenced to the sub-module mid-plane (Figure \ref{setup_VZLU}), which implies a theoretical co-focus of the stacked 2D assembly at \(F_{2\mathrm{D}} \approx 365~\mathrm{mm}\).

10. In Sec 6, two types of detectors are used. It is not clear which is obtained by Rigaku CMOS camera and which is by the Quad with EGSE for the results presented in Fig 11, 12, 13, and Table 4, 5. – Fig 11 and 12 already state in their captions that the data were measured with the spectrometer. Fig. 13 and to the notes of Tables 4 and 5 added „Data acquired with the spectrometer.“
11. Page 13, Fig 16, which energy is for NiP? – see 4 + added NiP (0.85 keV)
12. The ‘gain’ in Sec 6.5 should be the same as that in Sec 6.2. Should not it be simply A_eff/A_det ? If not, why?
    Sec. 6.2 – Data acquired with the spectrometer - G_nor(b) derived from spectrometer data in predefined energy bands; see 7
    Sec. 6.5 - Data acquired with the CMOS detector - which is not energy-resolving; it integrates the signal over the full source spectrum, gain was computed as the ratio of the global maximum in the optics ROI to the mean of the reference ROI (source image - without the optics).

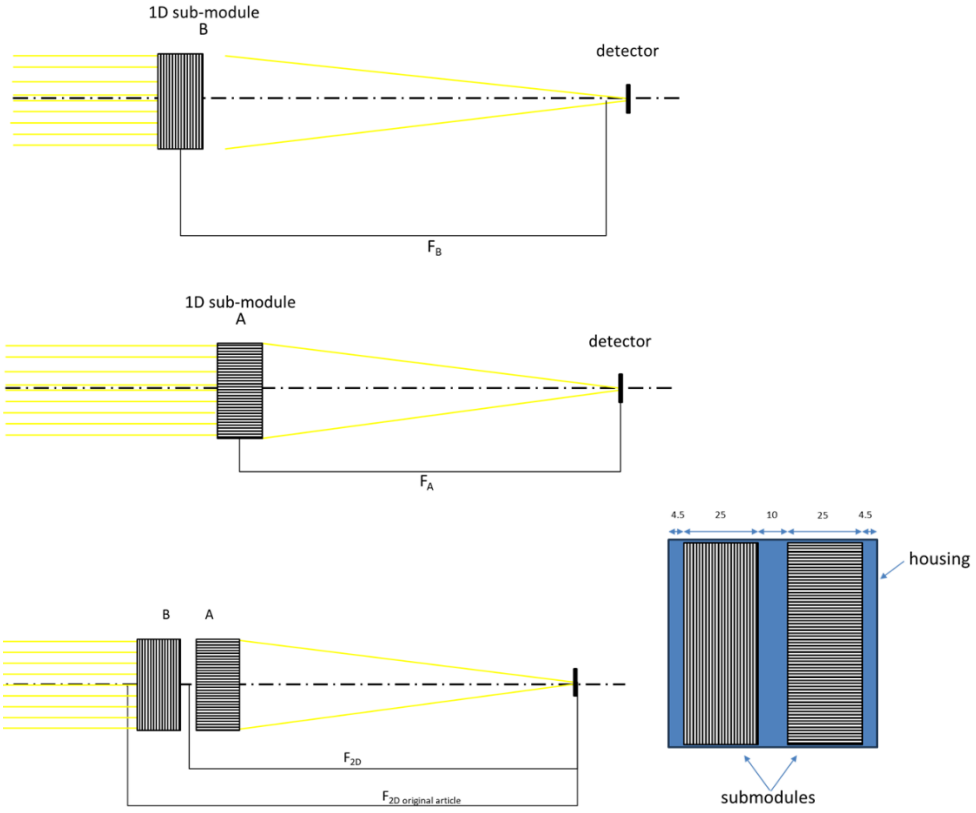
Added:
The gain G was calculated as the ratio of the global maximum in the optical ROI to the mean of the reference ROI_{ref} (source image - without the optics). This yields the peak-based gain of the optics relative to the average level of the direct beam. The gain was calculated using the following equation.
\begin{equation}
G_{\max}=\frac{\max(\mathrm{ROI_{cor}})}{\operatorname{mean}(\mathrm{ROI_{refcor}})},
\end{equation}
where ROI (Region of Interest) denotes a fixed subregion of the image containing the spot. The same ROI was used for the optics and the reference images. Both ROIs were background corrected (ROI_{cor}).

13. The relation between 'FoV' determination and 'Off-axis imaging' should be further elaborated.
    The off-axis imaging and FoV determination address different questions and are therefore not in direct correspondence.
    Off-axis imaging (Fig. 17) quantifies focus - specifically the FWHM of the focus spot and its broadening/asymmetry when the source is moved off axis.
    FoV determination (Fig. 14-15) establishes the maximum incidence angle at which the optics still deliver a usable image on the detector and geometric vignetting by the LE foils and supporting structures.
    Thus, off-axis imaging informs how the focus degrades, whereas the FoV boundary is set by signal intensity and geometric limits, not by a FWHM.
    Added:
    Off-axis imaging (Fig. ...) characterizes the FWHM and blur as a function of field angle (Fig. ...). By contrast, the FoV (Fig. ...) reported here is the range of incidence angles for which the focus image remains on the active detector area and the detected flux is above the usable signal value. Consequently, off-axis imaging describes the image quality (focus blurring), while the FoV edge is set primarily by geometric throughput limits rather than by a specific FWHM criterion.
    Plus sections 6.4 and 6.5 have been swapped so that FOV and Off axis are in sequence.
14. If possible, all measurements uncertainties should be shown in corresponding figures.
    Owing to the complexity of the laboratory setup and limited time, the number of repeats per configuration did not allow statistically meaningful error bars to be shown in all figures.

Dear,

thank you for the careful reading and constructive feedback. We address each point below and have revised the manuscript accordingly.

1. All figures must be referenced in the text. DONE
   Section 2
2. In the manuscript, the acronym MPO is used with two different meanings: Mercury Planetary Orbiter and micropore optics. The latter meaning is introduced twice in Section 2, with inconsistent writing — both “Micro-Pore Optics” and “micropore optics” are used. I recommend standardizing the term to a single form (e.g., “micropore optics”) and removing the first introduction of the acronym, as the Mercury Planetary Orbiter is not mentioned anywhere else in the paper. DONE
3. There is a wrong dot in “launch in 2025. extends". DONE
   Section 3
4. There is no need to re-enter the achronym MFO. DONE
5. Why do the submodules have different focal lengths (as shown in Table 1)? How is this difference adjusted when the submodules work together? Why do the focal length values in Section 6 differ from those shown in Table 1?
   The two 1D sub-modules (vertical and horizontal) are mounted in series along the optical axis - one sub-module sits upstream of the other that is why their nominal focal lengths are intentionally offset so that both foci land on the same detector plane (see Fig. 7).
   In practice, the difference needs to be at least the sub-module width to compensate the physical/geometrical offset.



In the original plots, the detector distance was measured from the edge of the optics/submodules during measurement. We re-referenced all distances to the submodule or 2D optics midplane, consistent with Sec. 3 or Fig. 7 (please see F_A, F_B and F_{2D}), and updated Figs. 9, 11, and 13 and Tab. 1.

During assembly we stack the 1D sub-modules “one behind the other”, set the detector plane, and use shims adjustments so that the vertical and horizontal foci coincide on the detector plane. The focal-length offset ensures this co-focus without extra optical elements.
The differences between the theoretical focal lengths and the measured best-focus distances are from manufacturing tolerances and assembly/alignment errors, the sub-modules are not ideal.

Added:
During co-focusing to form the 2D optics, the two 1D sub-modules are mounted in series along the optical axis. Sub-module A is located upstream of sub-module B. In order to position their linear focus on the same detector plane, the one sub-module is intentionally specified with a longer nominal focal length than the other. The required offset is greater than:

\begin{equation}
\Delta F \equiv F_A - F_B,
\label{DeltaF}
\end{equation}

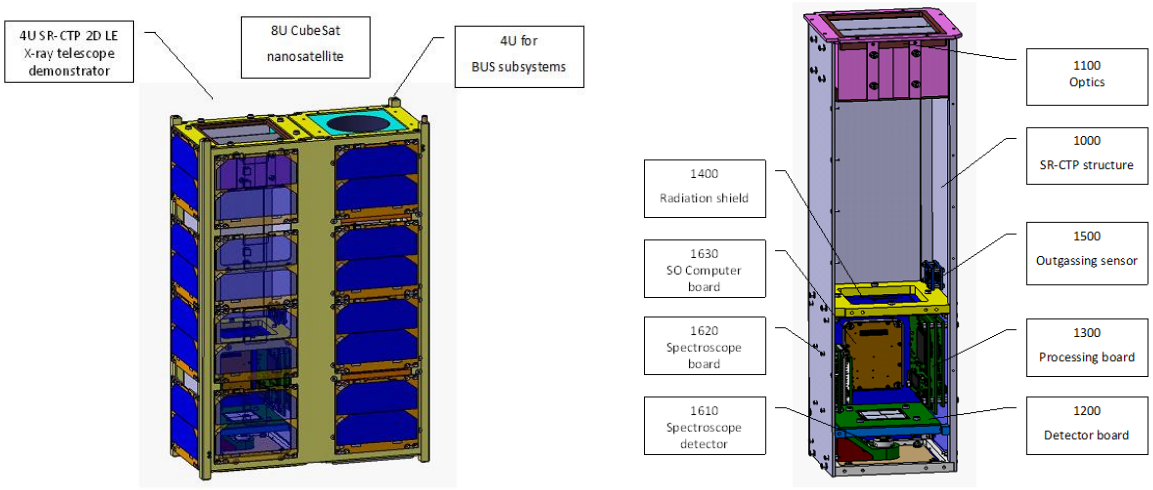
where \(F_A\) and \(F_B\) are the nominal focal lengths of the sub-modules and \(\Delta F\) is their minimal axial spacing (approximately the sub-module width). In practice, to accommodate assembly tolerances we use a safety margin and choose \(\Delta F + 10~\mathrm{mm}\), which ensures co-focus without additional optics.

Added - Section 6.1
X-ray vacuum testing was conducted to verify the key optical parameters of the LE system. Measurements were taken separately for each one-dimensional (1D) sub-module and then for the full two-dimensional (2D) assembly. To comply with the 4U CubeSat envelope (100 × 100 × 400 mm), the design nominal focal lengths were set to \(F_A = 347.5~\mathrm{mm}\) and \(F_B = 382.5~\mathrm{mm}\) (distances referenced to the sub-module mid-plane (Figure \ref{setup_VZLU}), which implies a theoretical co-focus of the stacked 2D assembly at \(F_{2\mathrm{D}} \approx 365~\mathrm{mm}\).

Section 4

6. The dimensions of the CubeSat demonstrator are indicated in 4U, however, when comparing the suggested sizes of the submodules and the detector system, it seems that the dimensions of the CubeSat demonstrator are smaller than 4U. This aspect needs to be clarified.
   The core element of the demonstrator is a compact 2D Lobster Eye X-ray telescope, developed by designed to fit within a 4U CubeSat form factor (10 cm × 10 cm × 40 cm), representing a single, self-contained payload module. The 4U LE payload integrates the subsystems required for autonomous operation, forming a complete X-ray telescope

unit. More details will be provided in the next article, where the implementation of the optics and testing of the entire X-ray demonstrator are described.



CubeSat design including the SR-CTP X-ray demonstrator (left) and SR-CTP X-ray demonstrator design (right).

Section 6

7. Please add to the text of Section 6 an explanation of which submodule (A or B) is horizontal, and which is vertical.
   Done – added/updated 6.1
   Before co-focusing the 2D assembly, sub-module A (vertical) and sub-module B (horizontal) were measured separately to determine (Figure \ref{LE_VZLU}) their actual best-focus distances (focal lengths) and angular resolution. The focal length and angular resolution were then verified using images of the focal spot. Horizontal and vertical full width at half maximum (FWHM) values were extracted to determine the optimal focus. In Figure~\ref{FWHM_NiP_graf}, the left panel shows FWHM versus detector distance (Gaussian fit), while the right panel shows the corresponding peak signal. Red markers denote the vertical direction and blue markers the horizontal direction. Data were acquired with the Rigaku CMOS camera (non–energy-resolving).
8. It is necessary to explain which row corresponds to which parameters in Fig.10.
   Done – caption updated
   \caption{Best-focus results with line profiles. Rows (top$\to$bottom): NiP target, Ag target, Ti target. Columns (left$\to$right): 2D focus image; vertical intensity profile; horizontal intensity profile (profiles taken through the focus maximum). Measured with the Rigaku CMOS detector (non–energy-resolving).}
9. In the plots in Figure 11, please replace the caption of the ordinate axes with “Intensity"
   DONE
10. Under which target angular resolution plot was constructed at Fig. 13?
    DONE – caption updated
    The dependence of angular resolution on the focal length was measured at 3.0 keV. Data acquired with the spectrometer.
11. There is a lack of conclusions on the performed measurements in subsection 6.4.
    Added: The FoV boundary is set primarily by geometric throughput limits—vignetting of the foils and supporting structures, e.i. the loss of usable signal occurs.

Plus added to the Off axis section:
Off-axis imaging (Fig. ...) characterizes the FWHM and blur as a function of field angle (Fig. ...). By contrast, the FoV (Fig. ...) reported here is the range of incidence angles for which the focus image remains on the active detector area and the detected flux is above the usable signal value. Consequently, off-axis imaging describes the image quality (focus blurring), while the FoV edge is set primarily by geometric throughput limits rather than by a specific FWHM criterion.